Journal of Bionic Engineering
https://doi.org/10.1007/s42235-025-00829-y

RESEARCH ARTICLE

Design and Implementation of the Bionic Webbed Feet for Thrust Efficiency Improvement Based on Surrogate-assisted Kinematic Characterization

Yan Niu[1] · Xinru Lin[1] · Shuxiang Guo[2,3] · Zhibin Song[4,5] · Liwei Shi[1,2]

Received: 12 August 2025 / Revised: 30 November 2025 / Accepted: 11 December 2025

Abstract
Despite advancements, amphibious robots still exhibit inadequate locomotion performance. As natatores demonstrate exceptional walking and swimming capabilities, they provide an ideal bionic prototype for structural enhancement. Consequently, this study designed a novel propulsion mechanism inspired by waterfowl, featuring a slider-four-bar linkage system that simultaneously enables foot folding and retracting. Static structural analysis was performed to identify and optimize weak components of the mechanism. The achievable workspace of the mechanism was calculated through kinematic analysis. Mathematical and numerical hydrodynamic models were established to evaluate the mechanism's hydrodynamic performance using a defined thrust efficiency metric. To analyze the influence of kinematic parameters on the propulsion mechanism across full motion cycles, a surrogate model correlating kinematic parameters with the thrust efficiency metric was developed. Results demonstrate that the optimized propulsion mechanism satisfies the requirement of static performance under working conditions. Compared to the Waterfowl-inspired robot-I (WIR-I), the proposed mechanism achieves reduction in retraction stroke resistance for robotic webbed-foot propulsion systems. Surrogate model results show the following hierarchy of influence across kinematic parameters on the thrust efficiency metric: Paddling angle per cycle exceeds temporal baseline, which in turn exceeds temporal scaling factor of extension phase, power stroke, flexion phase, and retraction stroke. Flow field characterization indicates that flow attachment constitutes the dominant factor governing thrust efficiency. These findings could provide new design principles for future biomimetic webbed-foot robotic systems and establish a theoretical foundation for hydrodynamic optimization in amphibious robotics development and deployment.

Keywords Propulsion mechanism design · Structural optimization · CFD simulation · Surrogate model · Kinematic strategy optimization

In this article, Zhibin song was not denoted as the corresponding author.

✉ Zhibin Song
songzhibin@tju.edu.cn

✉ Liwei Shi
shiliwei@bit.edu.cn

1 School of Medical Technology, Beijing Institute of Technology, Beijing 100081, China

2 Key Laboratory of Convergence Medical Engineering System and Healthcare Technology, Ministry of Industry and Information Technology, Beijing Institute of Technology, Beijing 100081, China

3 Department of Electronic and Electrical Engineering, Southern University of Science and Technology, Shenzhen 518055, Guangdong, China

4 School of Mechanical Engineering, Tianjin University, Tianjin 300350, China

5 Key Laboratory of Mechanism Theory and Equipment Design of Ministry of Education, Tianjin University, Tianjin 300350, China

Published online: 12 January 2026

1 Introduction

Bionics has inspired unconventional approaches in amphibious robotics, enabling these systems to perform increasingly challenging missions [1–5]. By analyzing the morphological structures and locomotion strategies of highly capable amphibious animals, researchers can execute optimization referring to them in amphibious robots [6].

Numerous amphibious robotics have been developed at present used for different missions. Snake-inspired robots [7–10] have excellent performance in confined spaces for exploration missions, owing to their morphological structures. Salamander-inspired robots [11, 12] exhibit rapid terrestrial-aquatic locomotion and agile maneuvering capabilities, demonstrating exceptional adaptability to swampy and littoral environments with seamless water-land transitions. However, high DOFs of the robots mentioned above make them challenging to control. Ray-inspired robots [13, 14] excel in efficient, stealthy underwater propulsion with minimal ecological disturbance but face challenges in high development costs and operational limitations in extreme conditions. Turtle-inspired robots [15–19] achieve unique amphibious locomotion functionality, but are constrained by slow speed and limited deep-water agility.

Species with webbed-foot exhibit high amphibious adaptability coupled with morphological simplicity, making them ideal archetypes for efficient bio-inspired robotics design. Taking waterfowl as an example, researchers have extensively analyzed the typical kinematic gait patterns of their webbed feet during underwater locomotion and pointed out that the paddling motion closely resembles that of a paddle blade [20–23]. Based on this hypothesis, a primary structure design objective for waterfowl-inspired robots is to maximize propulsion efficiency by minimizing drag and concurrently augmenting thrust during the paddling cycle. Although robots using webbed foot are rare, there are still some scholars studying the structure about changing the area of webbed foot during motion. Pandey et al. [24] use crank-slider mechanisms linking five digital bones to deploy or retract webbing foot, reducing motion resistance during swimming. Chen et al. [25] use cable-driven foot flexion to reduce resistance during recovery phases for beaver-inspired robot. But the webbed foot of the above robots can only employ the single-DoF kinematic transformation, which fails to achieve maximum drag reduction. Kashem et al. [26] use underactuated webbed foot with dual hinges. Hydrodynamics autonomously opens webbed foot during backward strokes and closes it during forward strokes for duck-inspired robot. But this mechanism does not allow for the area of the webbed foot changing and direct reverse movement of the robot. So, this paper focus on a waterfowl-inspired robot, employing a novel mechanism to reduce the drag as much as possible.

Furthermore, the gait pattern is a key determinant of the propulsion capability in webbed-foot mechanisms. Due to the hydrodynamic complexity of underwater environments, amphibious robots suffer complex force interactions during aquatic locomotion. Optimized gait can enhance the propulsion performance of webbed feet [27, 28]. However, Nonlinear fluid-structure hydrodynamic should be considered for identifying optimal kinematic parameter combinations Theoretical computational methods typically encompass mathematical models, numerical models, and surrogate models [29]. For complex fluid condition, mathematical models often fail to get precise results. Numerical modeling relies on Computational Fluid Dynamics (CFD). For example, Chen et al. [30] develope an index for underwater propulsion mechanisms, employing CFD to analyze the paddling characteristics of designed webbed feet. Compared with mathematical models, the CFD results provide trajectory optimizations to enhance thrust efficiency. Extant CFD studies mainly establish discrete mappings between parameters and performance metrics rather than continuous functional relationships. Critically, computational burden arises during multi-variable optimization due to direct CFD solution [31].

Surrogate-Based Optimization (SBO) algorithms have been developed to overcome the limitations of direct simulation [32, 33]. By integrating discrete numerical or experimental datasets into surrogate frameworks, high-fidelity continuous model of system is generated across the parameter space. SBO algorithms are now extensively applied in fluid-structure optimization problems [34–36]. Liu et al. adopte SBO to maximize the lift-to-drag ratio of ray-inspired robotic, simultaneously optimizing geometric curvature and kinematic parameters [37]. Gao et al. employe SBO to get hydrofoil profiles maximizing lift coefficient and lift-to-drag ratio. They use CFD-generated datasets to train surrogate models and give the optimization of each parameters [38].

To sum up, current biomimetic robotic with webbed feet predominantly employ single adaptation strategies, such as reducing area of webbed foot or only flexion, which fails to fully mimic the features observed in biological systems. This limitation do not well reduce the detrimental drag forces during motion. Building upon Waterfowl-inspired robot-I (WIR-I), this work proposed a novel webbed-foot propulsion mechanism to improve the propulsion efficiency. Static simulations and optimizations were performed on the designed mechanism components. Hydrodynamic performance metrics were formulated to evaluate the impact of motion parameters on hydrodynamic performance. To reduce computational costs in hydrodynamic analysis

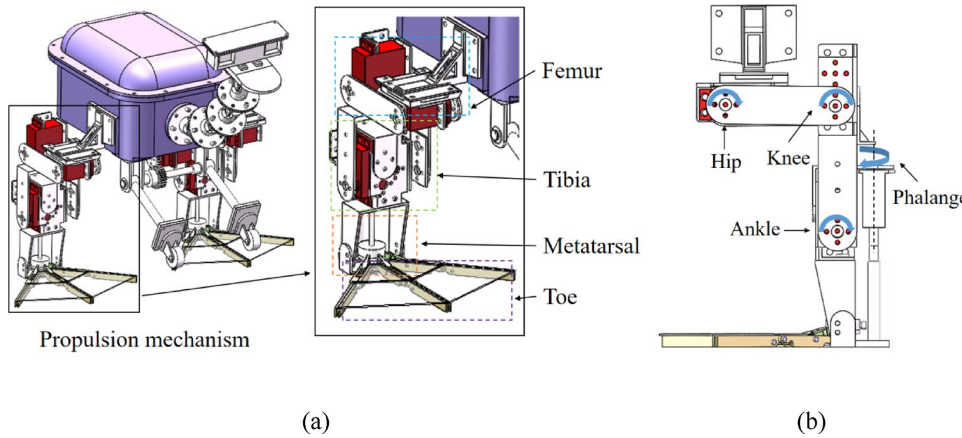

Fig. 1 WIR-II platform **a** Overall structure **b** Propulsive structure

Table 1 Parameters of the propulsion mechanism

Part	Length/mm	Range of motion/°
Femur	90	[-40,40]
Tibia	132	[-60,120]
Toes	142	[-45,135]

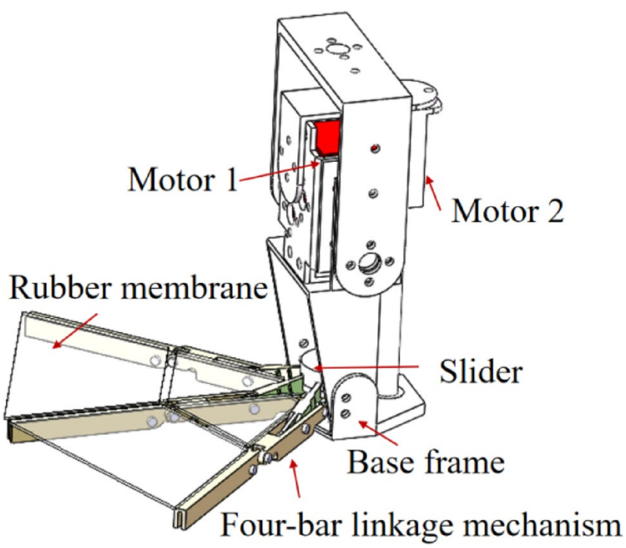

Fig. 2 Structure of webbed foot in WIR-II

and avoid local solution, theoretical and simulation-based hydrodynamic models were established for the webbed foot, generating discrete motion data across full cycles. A surrogate model linking kinematic parameters to propulsion performance metrics was developed to analyze how motion parameters influence propulsion efficiency. Based on this framework, the impact of motion parameters on propulsion performance was investigated, enabling optimization of the webbed-foot mechanism's motion strategy.

Key contributes of this paper include:

(1) A novel webbed-foot mechanism inspired by waterfowl was proposed to address the problem of excessive harmful resistance in underwater environment.
(2) An optimization of the webbed feet based on static analysis was carried out to make the mechanism meet the requirement under working condition.
(3) A surrogate model linking kinematic parameters to thrust efficiency was developed using the discrete hydrodynamic data from simulation to reduce the computational costs.
(4) The impact of motion parameters on thrust efficiency was analyzed to optimize the gait of paddling in underwater environment.

The rest of this paper are as follows. In Sect. 2, the propulsion mechanism of waterfowl-inspired robot is introduced and the optimization of structure through static performance was carried out. In Sect. 3, the kinematic model of propulsion mechanism was analyzed. In Sect. 4, the hydrodynamic performance was analyzed. In Sect. 5, the surrogate model of hydrodynamics was introduced and the strategy of motion was proposed. Finally, the conclusion and future work were given in Sect. 6.

2 Design of Propulsion Mechanism for Waterfowl-inspired Robot

2.1 Waterfowl-inspired Robot Platform

The WIR-I [39, 40] fails to fully fold its webbed feet during movement, which resulted in more resistance during webbed foot retraction. So, this paper proposed a new design named waterfowl-inspired robot-II(WIR-II). Figure 1 shows the structure of WIR-II. The propulsive structure consists of the femur, tibia, metatarsal and toes, which possesses 4 degree of freedom. Table 1 shows the parameters of the propulsion mechanism.

Figure 2 shows the structure of the webbed foot. The webbed foot of WIR-II comprises three toe bones. Each bone is constructed from a four-bar linkage mechanism.

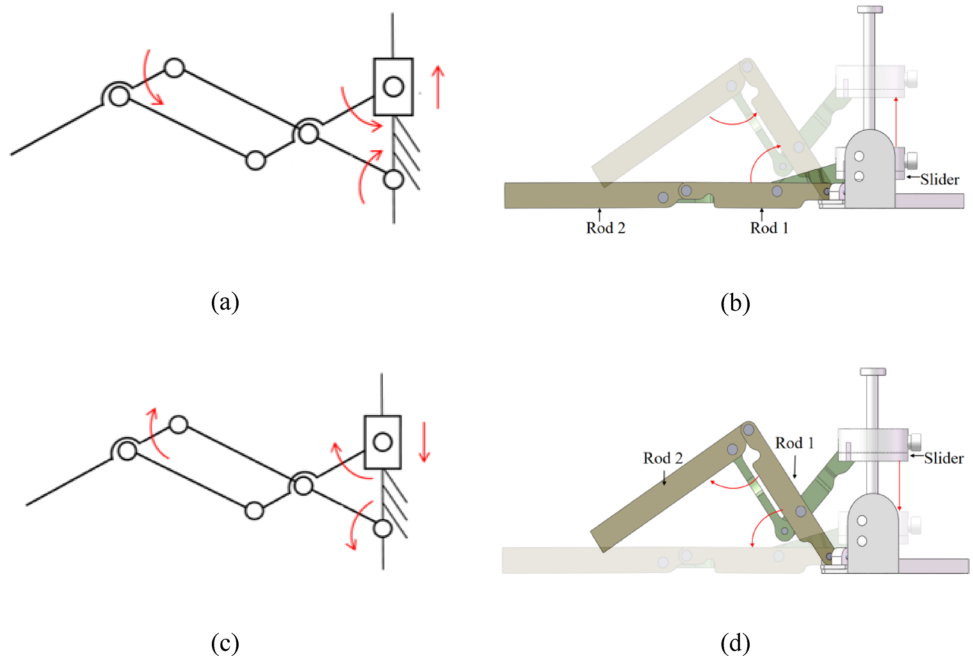

Fig. 3 Operating principle of webbed foot in WIR-II **a** Side view of expanding for kinematical diagram of mechanism **b** Side view of expanding for virtual prototype diagram **c** Top view of folding for kinematical diagram of mechanism **d** Top view of folding for virtual prototype diagram

Table 2 Material properties

Properties	Value
Density	7850 kg/m3
Young's modulus	200GPa
Poisson's ratio	0.3
Yield stress	250 MPa
Safety factor	2

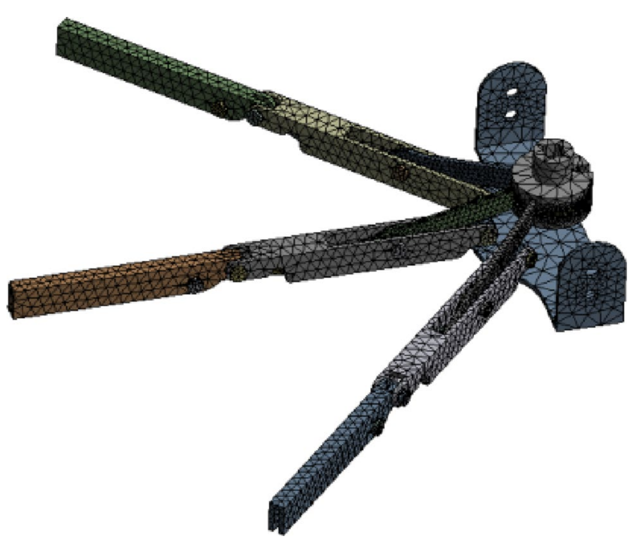

Fig. 4 FEM of webbed foot

These three sets of toes are interconnected through sliders and a base frame, with this part overlaid by a flexible rubber membrane. The webbed foot is equipped with two motors which drive the overall rotation and folding motion of the webbed foot. Compared to the WIR-I, WIR-II increases the degree of freedom of the webbed foot without requiring additional motors.

Figure 3 shows the operating principle of webbed foot in WIR-II. During the procedure of the retraction stroke (Fig. 3a-b), the slider moves upwards, driving Rod 1 clockwise and Rod 2 counterclockwise to fold the rubber membrane up. This reduces the effective propulsive area, thereby minimizing drag in this stroke. Vice versa, during the power stroke(Fig. 3c-d), downward slider motion rotates Rod 1 counterclockwise and Rod 2 clockwise, deploying the membrane to maximize the thrust-generating area for enhanced propulsion in the power stroke.

2.2 Static Structural Analysis

To ensure that the propulsion mechanism does not fail during operation, static structural analysis of the WIR-II's webbed foot mechanism was carried out within ANSYS. Table 2 shows the material properties of finite element model(FEM). The contact surfaces use the Coulomb friction whose coefficient is 0.17. A mesh independence study was conducted with the maximum von Mises stress as the convergence criterion. The number of mesh of FEM is converged at 40,873 and the model is shown in Fig. 4.

This study focuses on validating the performance of the webbed foot mechanism during the power stroke. Based on literature [41], the analysis was conducted with applying a surface-normal force of 20 N on the webbed foot.

Figure 5(a) and (c) show the deformation and von Mises stress results of the original mechanism. The max deformation was 5.83 mm which was less than 5% of the toe length,

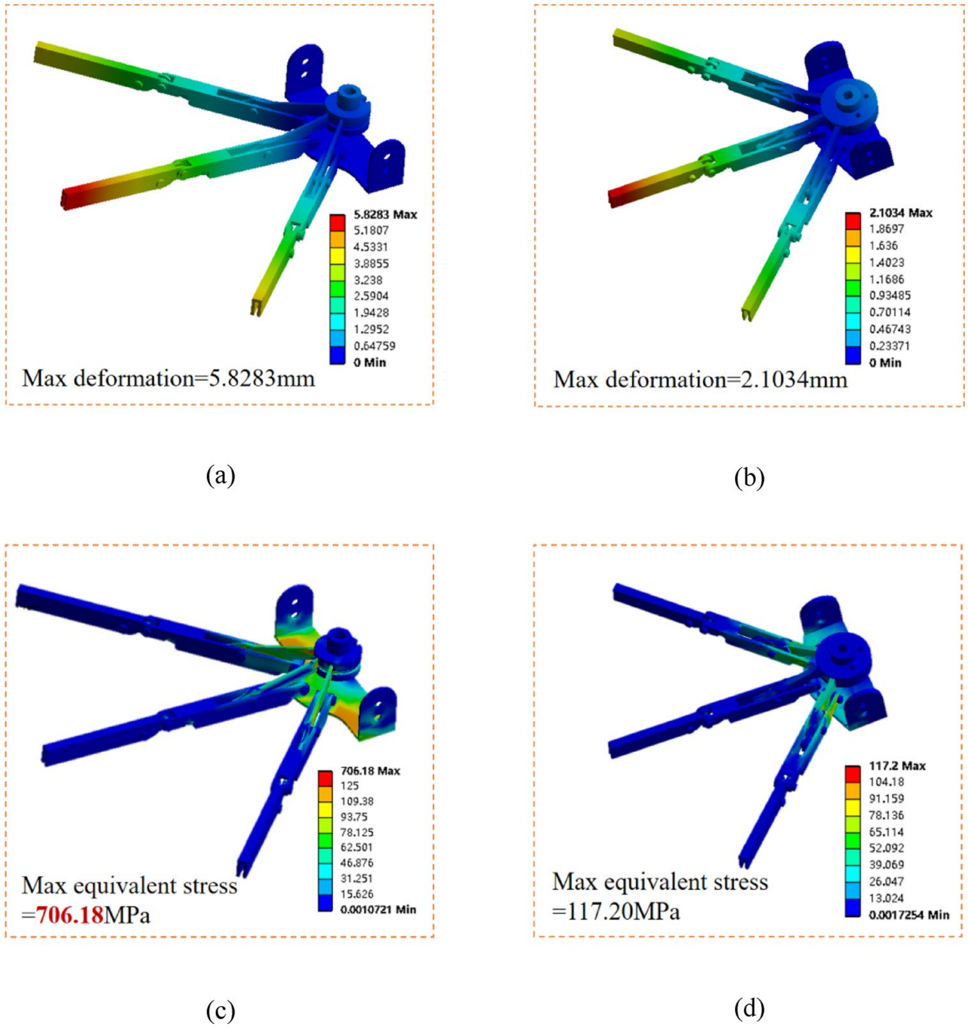

Fig. 5 Results of static performance before and after optimization of webbed foot mechanism **a** deformation of webbed foot before optimization **b** deformation of webbed foot after optimization **c** equivalent stress of webbed foot before optimization **d** equivalent stress of webbed foot after optimization

so the deformation met the requirement. But the maximum von Mises stress indicated critically insufficient strength. So, the red zones need to be redesigned. The results of structural optimization are shown in Fig. 6, including thickening of critical sections while maintaining non-interference conditions with adjacent linkages. Furthermore, the diameter of the hole where large stress occurred was enlarged. The significant stress reduction with seemingly minor geometric changes is primarily attributable to the mitigation of stress concentration. The von Mises stress of post-optimization parts decreased from 674.25 MPa, 210.33 MPa, and 371.20 MPa to 84.00 MPa, 88.74 MPa, and 18.11 MPa, respectively, which were all below the allowable stress of 125 MPa, meeting the strength requirement in this working condition.

The static performance of the webbed foot mechanism which comprised the post-optimization parts was verified with 98,890 elements according to the mesh independence study, as is shown in Fig. 5(b) and (d). The maximum von Mises stress reduced from 706.18 MPa to 117.20 MPa, which met the strength requirement.

2.3 Prototype

A prototype was manufactured according to the optimized structure. The prototype of webbed foot in WIR-II is shown in Fig. 7. The prototype which was used to verify the motion in one cycle was fixed by a bracket. The experiment was carried out in a pool whose size was 1.2 m, 0.4 m and 0.6 m.

3 Kinematic Model of Propulsive Structure

The propulsion mechanism of the WIR-II can be simplified into the model depicted in Fig. 8(a). Three gray cylinders represent motors and pentagrams denote foot-tip position. The length of femur, tibia, metatarsal and phalanges is l_1, l_2, l_3, and l_4 respectively.

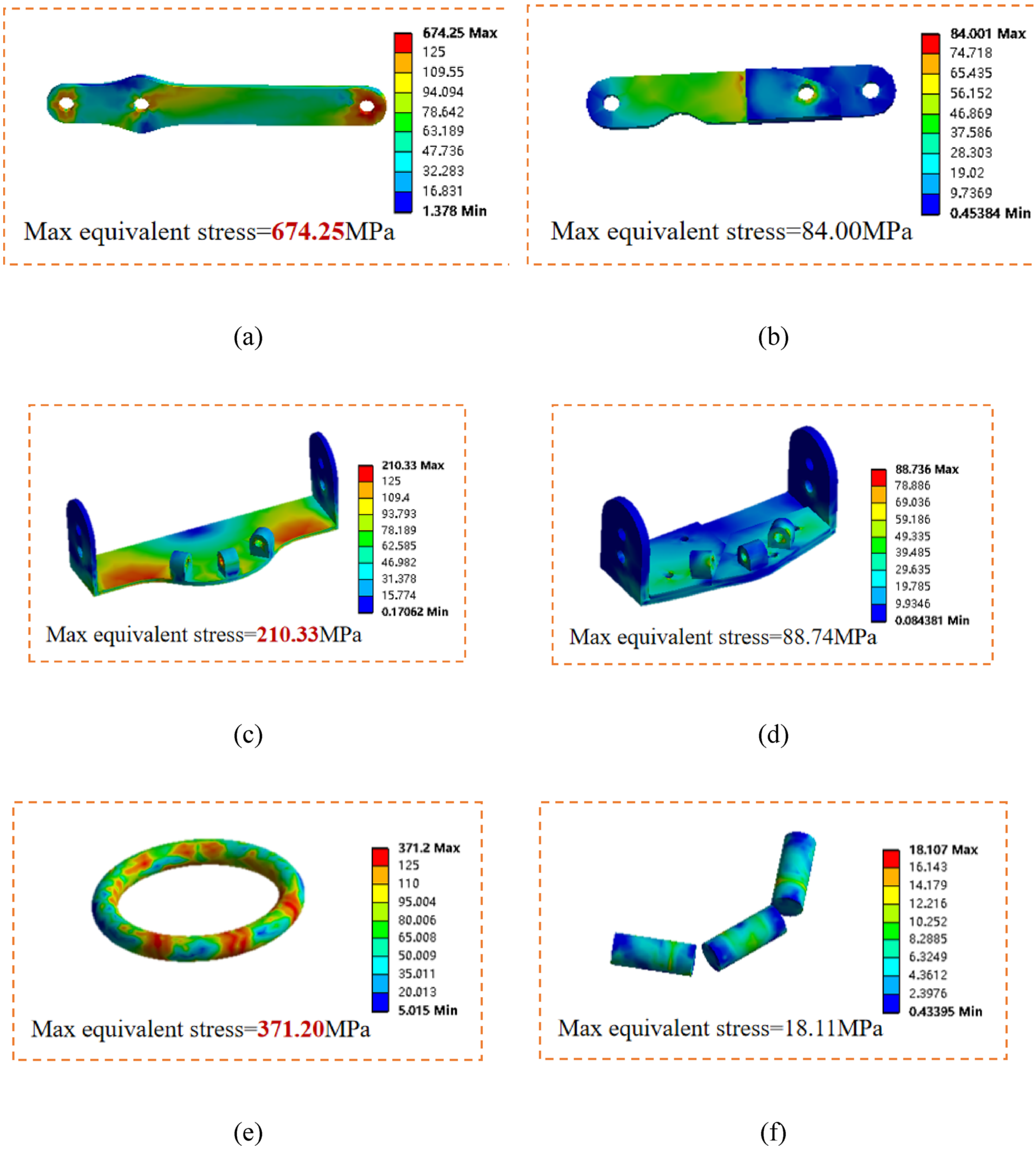

Fig. 6 Results of von Mises stress before and after optimization of critical parts **a** linkage before optimization **b** linkage after optimization **c** base frame before optimization **d** base frame after optimization **e** connecting axle before optimization **f** connecting axle after optimization

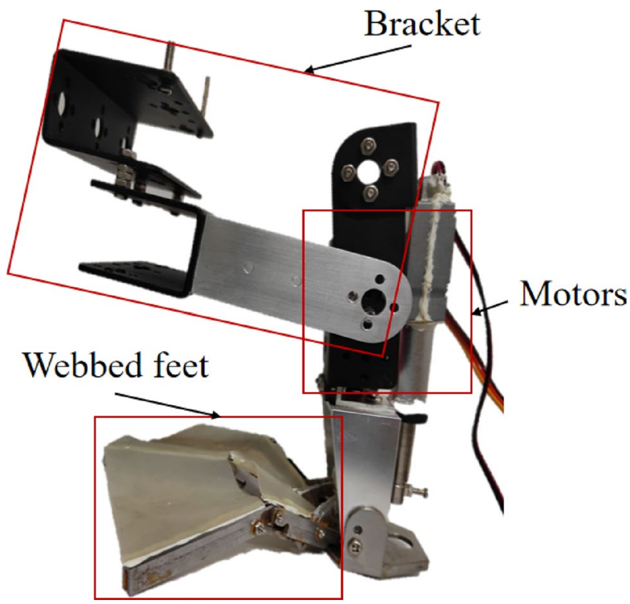

Fig. 7 The prototype of webbed foot in WIR-II

The kinematic model shown in Fig. 8(b) was constructed with the base frame O_0 fixed at the hip joint. Since all motor rotation axes were perpendicular to the same plane, all joint *Z*-axis were assigned normal to the plane of motion (outward from the page). The *X*-axis of joint *i* points toward the center of the next joint *i*+1. The *X*-axis of the terminal joint was along the direction of l_4 and the positive direction was the same as motion. *Y*-axis follow the right-hand rule convention. Denavit-Hartenberg(D-H) parameters are summarized in Table 3.

Forward kinematics analysis was carried out and the transformation matrices ${}_0{}^1\boldsymbol{T}$, ${}_1{}^2\boldsymbol{T}$, ${}_2{}^3\boldsymbol{T}$ are obtained as follows

Table 3 D-H parameters of WIR-II

Linkage i	a_i/mm	d_i/mm	α_i/°	θ_i/°
1	l_1	0	0	θ_1
2	l_2	0	0	θ_2
3	$\sqrt{l_3^2 + l_4^2}$	0	0	θ_3

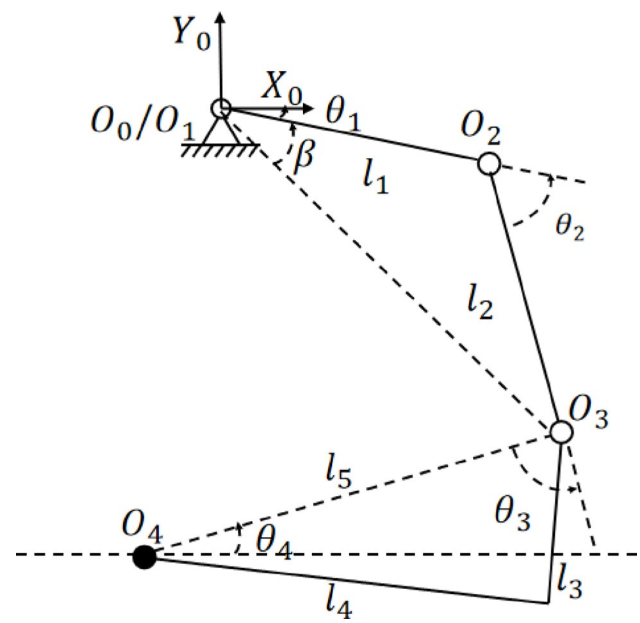

Fig. 9 Simplified diagram of propulsion mechanism of WIR-II

$$
{}_0{}^1\boldsymbol{T} = \begin{bmatrix} c\theta_1 & -s\theta_1 & 0 & l_1 c\theta_1 \\ s\theta_1 & c\theta_1 & 0 & l_1 s\theta_1 \\ 0 & 0 & 1 & 0 \\ 0 & 0 & 0 & 1 \end{bmatrix} \tag{1}
$$

$$
{}_1{}^2\boldsymbol{T} = \begin{bmatrix} c\theta_2 & -s\theta_2 & 0 & l_2 c\theta_2 \\ s\theta_2 & c\theta_2 & 0 & l_2 s\theta_2 \\ 0 & 0 & 1 & 0 \\ 0 & 0 & 0 & 1 \end{bmatrix} \tag{2}
$$

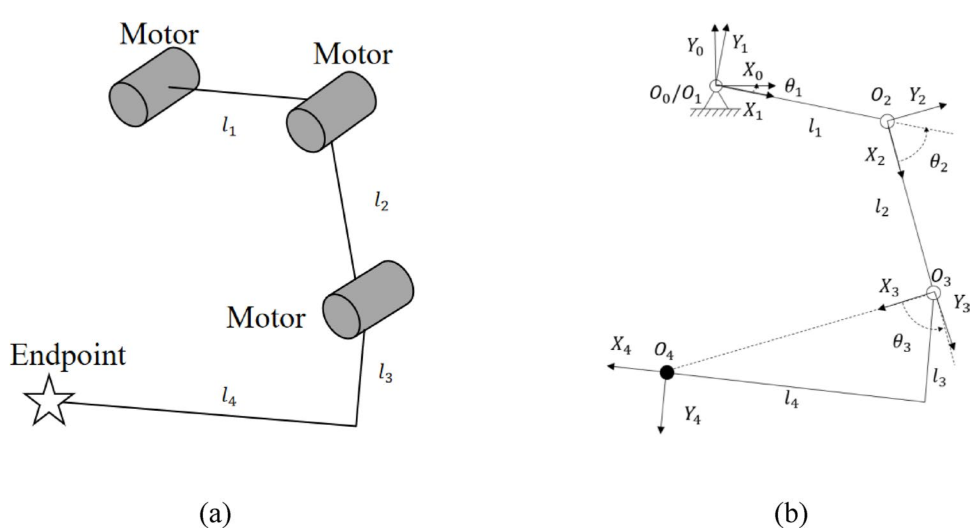

Fig. 8 The schematic diagram of the propulsion mechanism. **a** simplified model of the leg, **b** the parameters involved in the kinematic analysis

$$ {}_2^3\boldsymbol{T} = \begin{bmatrix} c\theta_3 & -s\theta_3 & 0 & l_5 c\theta_3 \\ s\theta_3 & c\theta_3 & 0 & l_5 s\theta_3 \\ 0 & 0 & 1 & 0 \\ 0 & 0 & 0 & 1 \end{bmatrix} \tag{3} $$

where $c\theta_i$ denotes $cos\theta_i$ and $s\theta_i$ denotes $sin\theta_i$. $l_5 = \sqrt{l_3^2 + l_4^2}$ is the distance between O_3 and O_4, shown in Fig. 9. The homogeneous transformation matrix from the base coordinate frame (i=0) to the third coordinate frame (i=3), denotes as ${}_0^3\boldsymbol{T}$, is computed by the chain product of successive transformations:

$$ \begin{aligned} {}_0^3T &= {}_0^1T \times {}_1^2T \times {}_2^3T \\ &= \begin{bmatrix} c\theta_{1+2+3} & -s\theta_{1+2+3} & 0 & l_1c\theta_1 + l_2c\theta_{1+2} + l_5c\theta_{1+2+3} \\ s\theta_{1+2+3} & c\theta_{1+2+3} & 0 & l_1s\theta_1 + l_2s\theta_{1+2} + l_5s\theta_{1+2+3} \\ 0 & 0 & 1 & 0 \\ 0 & 0 & 0 & 1 \end{bmatrix} \end{aligned} \tag{4} $$

where θ_{1+2+3} denotes $\theta_1 + \theta_2 + \theta_3$ and θ_{1+2} denotes $\theta_1 + \theta_2$.

Inverse kinematics was solved via a geometric approach. As shown in Fig. 9, joint angles cannot be uniquely determined with only the end-effector position specified. When partial joint angles or geometric constraints were provided, the remaining variables became solvable. So, with known link lengths of l_1- l_5, position of O_4 and the angle θ_4 between link l_5 and the horizontal plane, θ_1、 θ_2 and θ_3 were derived as follows.

The coordinate of $O_3(x_3, y_3)$ can be obtained firstly

$$ \begin{cases} x_3 = x_4 + l_5 cos\theta_4 \\ y_3 = y_4 + l_5 sin\theta_4 \end{cases} \tag{5} $$

In $\Delta O_1O_2O_3$, θ_2 and β is derived as follows:

$$ \theta_2 = arccos\left(\frac{x_3^2+y_3^2-l_1^2-l_2^2}{2l_1l_2}\right) \tag{6} $$

$$ \beta = arccos\left(\frac{x_3^2+y_3^2+l_1^2-l_2^2}{2l_1\sqrt{x_3^2+y_3^2}}\right) \tag{7} $$

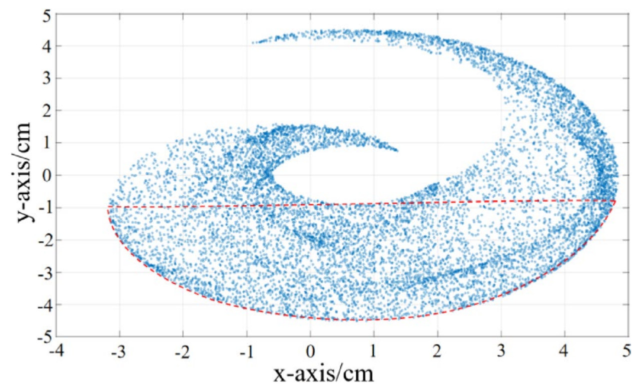

Fig. 10 The reachable workspace of the WIR-II propulsion mechanism

θ_1 which was determined according to the coordinate of O_3 and β. θ_3 is computed by:

$$ \theta_3 = \pi - (\theta_1 + \theta_2 + \theta_4) \tag{8} $$

The reachable workspace of the WIR-II propulsion mechanism is shown in Fig. 10. The fan-shaped shown as dash line quantifies the maximum stroke span and clearance height per cycle.

4 Hydrodynamic Performance Analysis

4.1 Theoretical Model

A schematic structural diagram of the webbed foot mechanism in WIR-II and WIR-I is shown in Fig. 11. The webbed foot was divided into base, membrane 1 and membrane 2. The total hydrodynamic force F acting on the entire

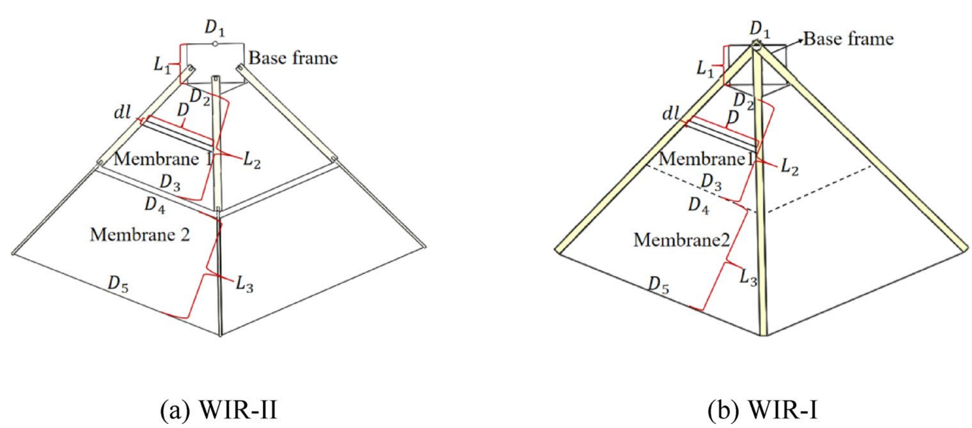

Fig. 11 The schematic structural diagram of the webbed foot

Table 4 Results of particle density independence verification

Far/near field particle size(m)	Thrust efficiency/%	Error of adjacent results/%
0.03/0.015	48.29	-
0.02/0.010	51.31	6.25
0.015/0.0075	56.11	9.35
0.01/0.005	58.7	4.62
0.006/0.003	60.36	2.83

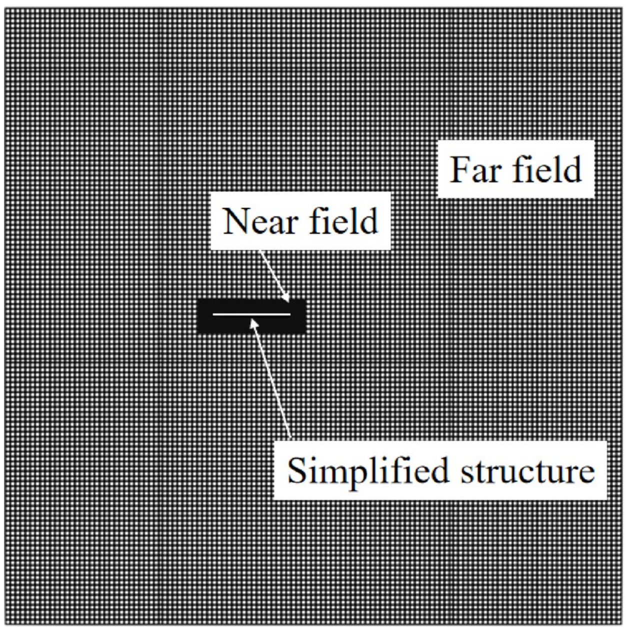

Fig. 12 Lattice field for simulation of webbed foot

webbed foot mechanism can be represented by the sum of hydrodynamic forces acting on its components:

$$F = F_1 + 2F_2 + 2F_3 \tag{9}$$

where F_1, F_2 and F_3 denotes the hydrodynamic force acting on base, membrane 1 and membrane 2 respectively.

The membrane thickness (1 mm) is substantially smaller than its planar dimensions, the added mass force becomes negligible. According to Morison equation, the force differential dF can be approximated as:

$$dF = \frac{1}{2} C_D \rho\, v\,|v|\, Ddl \tag{10}$$

Where C_D denotes the coefficient of drag, ρ denotes the density of medium, v denotes the linear velocity, D denotes the length of parallel side, dl denotes the differential length element.

So, F_1, F_2 and F_3 are obtained as follows:

$$F_1 = \frac{1}{2} C_D \rho \int_0^{L_1} v\,|v|\, D_1 dl \tag{11}$$

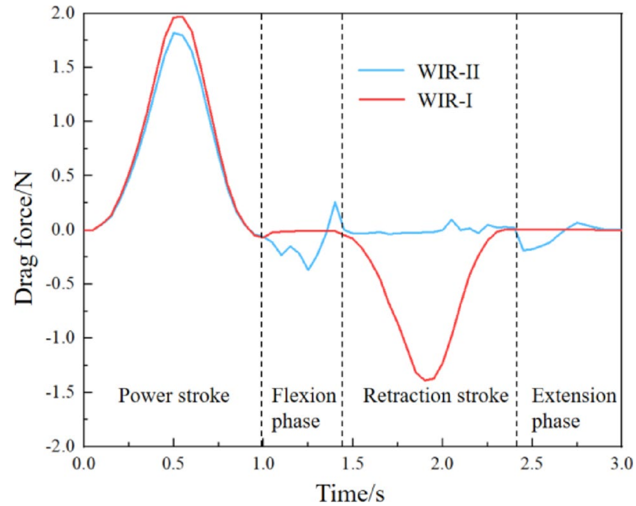

Fig. 13 Comparison of drag between WIR-II and WIR-I

$$F_2 = \frac{1}{2} C_D \rho \int_0^{L_2} v\,|v| \left(\frac{D_3 - D_2}{L_2} l + D_2\right) dl \tag{12}$$

$$F_3 = \frac{1}{2} C_D \rho \int_0^{L_3} v\,|v| \left(\frac{D_5 - D_4}{L_3} l + D_4\right) dl \tag{13}$$

where D_1- D_5 and L_1- L_3 denote the parallel side and the height of all the components respectively, as shown in Fig. 11. When the webbed foot is paddling, all components share the same angular velocity ω_0. The hydrodynamic force acting on a single webbed foot is computed by:

$$\begin{aligned} F = C_D \rho \,[\tfrac{1}{2} \textstyle\int_0^{L_1} (v_a - \omega_0 l)\,|v_a - \omega_0 l|\, D_1 dl \\ + \textstyle\int_0^{L_2} (v_a - \omega_0 l - \omega_0 L_1)\,|v_a - \omega_0 l - \omega_0 L_1| \left(\tfrac{D_3 - D_2}{L_2} l + D_2\right) dl \\ + \textstyle\int_0^{L_3} (v_a - \omega_0 l - \omega_0 L_{1+2})\,|v_a - \omega_0 l - \omega_0 L_{1+2}| \left(\tfrac{D_5 - D_4}{L_3} l + D_4\right) dl] \end{aligned} \tag{14}$$

A dimensionless thrust efficiency η is defined to quantify propulsion performance:

$$\eta = \frac{\sum F(t) \cdot \Delta t}{\sum |F(t)| \cdot \Delta t} \times 100\% \tag{15}$$

Where Δt denotes the time step.

4.2 CFD Model

The propulsion performance was simulated via xFlow which uses Lattice Boltzmann Method (LBM). Particle density independence verification was carried out and results are shown in Table 4. The verification converges at the size of 0.01/0.005 for far/near field particle size. The lattice field is shown in Fig. 12.

The webbed foot kinematics were defined using the STEP function in Adams to generate discrete-time pose data, which was subsequently imported into xFlow for simulation. The simulation was performed within a rectangular domain with a side length of 1 m. All domain boundaries except inlet/outlet were assigned no-slip impermeable wall conditions. The numerical simulation used an external single-phase flow model with forced incompressibility treatment. Fluid properties emulate liquid water at 288.15 K. The environment was still water. A Newtonian viscous constitutive model was adopted to resolve the laminar-turbulent mixed flow regime.

4.3 Results

The drag of the WIR-II and WIR-I is shown in Fig. 13. The total gait cycle takes 3 s, which is divided into four phases, 1 s for power stroke phase, 0.4s for flexion phase, 1 s for retraction stroke phase and 0.6s for extension phase.

During the power stroke, the hydrodynamic curves of both designs exhibited a rise-fall profile, but differing in peak value. The WIR-II demonstrated reduced peak drag which was 19% lower than WIR-I due to the separation gap between membrane 1 and 2. During the retraction stroke, the WIR-II exhibited less force fluctuations and the drag was close to zero, while the WIR-I displayed a distinct negative force profile characterized by an initial decline followed by an increase. The above results showed that WIR-II could reduce the detrimental drag efficiently.

Figure 14 shows the results of static pressure and velocity vectors at cross-section $x=0$ for the WIR-I and WIR-II webbed foot mechanisms respectively, which is at the time of 0.6s, 1.2s, 1.9s and 2.7s.

During the power stroke ($t=0.6$s), the webbed foot pushed against the fluid, resulting in the formation of a high-pressure zone on its leeward side. Meanwhile, as the flow accelerated around the foot to reach the windward side, a low-pressure zone was created. The above phenomenon was governed by Bernoulli's principle. This pressure distribution generated a pressure differential directed from the leeward side toward the windward side, which aligned with the direction of motion and thereby produced thrust. When fully deployed, the webbed foot of both WIR-I and WIR-II exhibited similar effective projected areas, meaning their maximum thrust capabilities were comparable. Throughout this phase, the flow remained fully attached.

At flexion phase ($t=1.2$ s), the pressure differential of WIR-II was significantly greater than that of WIR-I, because the larger, more aggressive motion of the folded foot actively energizes the flow field, inevitably inducing stronger local vortices and pressure fluctuations. However, this significant local pressure difference did not translate into a larger amplitude of drag, because the symmetrical shape presented by the webbed foot of WIR-II during flexion phase resulted in smaller component forces in the direction of motion from the pressures generated on both parts of the foot. Nevertheless, it could not completely avoid locally larger fluctuations in drag. The flow separation which induced vortex shedding causing force oscillations occurred at the WIR-II mechanism, whereas the WIR-I kept attached flow with forces close to zero.

Transitioning to retraction stroke ($t=1.9$ s), the webbed foot must push away the water ahead, resulting in a significant pressure increase on the windward side and forming a high-pressure zone. Simultaneously, flow separation occurs at the edge of the webbed foot, leading to the formation of vortices and a separation region on the leeward side, where pressure drops markedly to form a low-pressure zone. This pressure distribution creates a pressure differential directed from the windward to the leeward side, which acts as a drag force opposing the direction of motion. In the folded state, WIR-II contracts the webbed foot into a configuration that is more streamlined than that of WIR-I. This streamlined shape guides flow more smoothly around the foot, significantly mitigating flow separation and thereby preventing the formation of a large, unsteady low-pressure vortex region on the leeward side. Furthermore, in the flexion state, WIR-I has a larger effective projected area compared to WIR-II, meaning it must displace a greater volume of water. This amplifies flow disturbance and intensifies the high-pressure zone, resulting in a much larger pressure differential for WIR-I than for WIR-II. This corresponds to the negative force shown in Fig. 13. Localized flow separation occurred due to the folding motion of toes in the WIR-II, inducing unsteady hydrodynamic forces. However, both the pressure gradient value and vorticity levels were significantly reduced compared to the flexion phase, resulting in smaller force fluctuation amplitudes.

Similar to the flexion phase, during the extension phase ($t=2.7$ s), the pressure differential was negligible in WIR-I, which maintained attached flow across its surface. Conversely, the extension motion of WIR-II resulted in a greater pressure differential compared to WIR-I, with flow separation occurring at both the trailing edge and the phalangeal flexion joints, leading to significant energy dissipation.

Figure 15 shows the propulsion efficiency of webbed foot under different inlet velocities. The larger paddling angle can generate greater thrust, leading to higher thrust efficiency. As the inlet velocity increased, the efficiency decreased. According to the Morison's equation, larger inlet velocity led to greater drag, resulting in smaller thrust and the efficiency. When the inlet velocity was 0.3 m/s, the efficiency under the motion of 90 ° and 135 ° was very low, the thrust generated by the webbed foot at this speed struggles to overcome the drag, resulting in extremely low propulsion efficiency. So, the paddling angle in one cycle should be different with inlet velocities. The high efficiency will occur when the paddling velocity is far larger than inlet velocity.

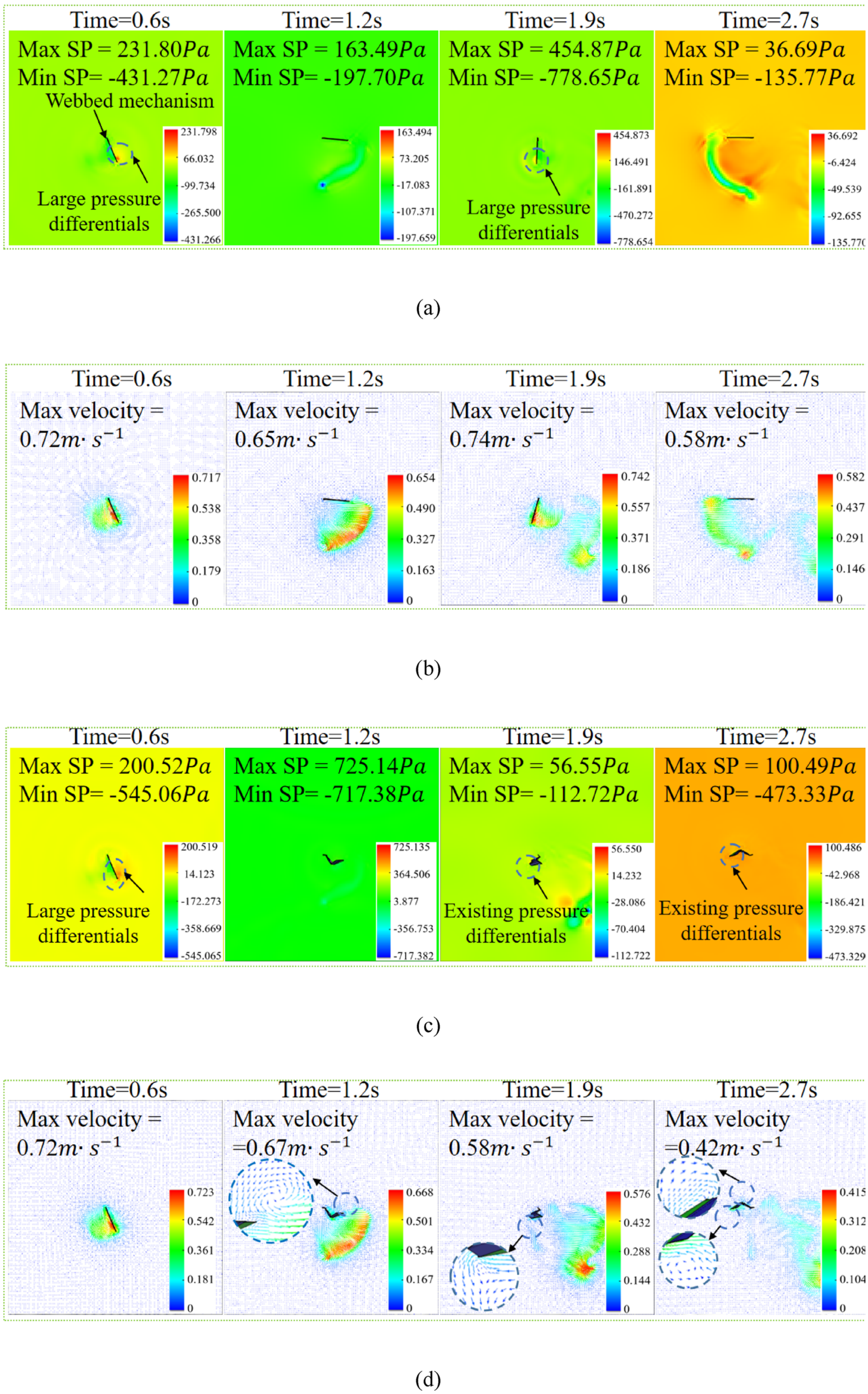

Fig. 14 Results at cross-section $x=0$ for the WIR-I and WIR-II **a** static pressure of WIR-I **b** velocity vectors of WIR-I **c** static pressure of WIR-II **d** velocity vectors of WIR-II

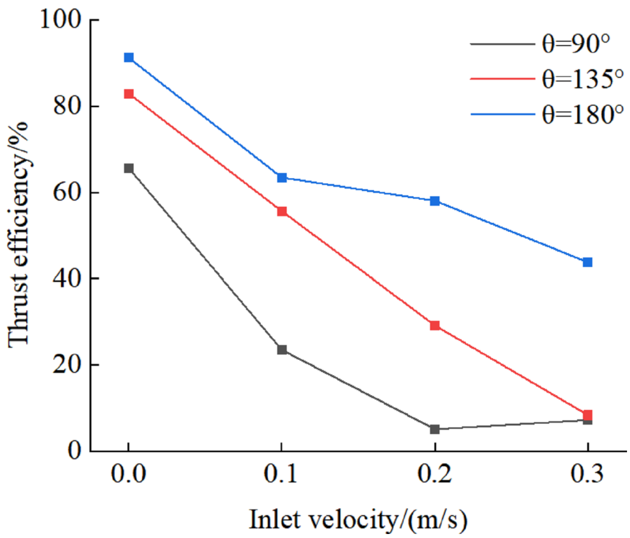

Fig. 15 Propulsion efficiency under different inlet velocities

The experiment results are shown in Fig. 16. The time of one cycle was 1.6s. the webbed feet moved according to the operating principle. When in the power stoke, the webbed feet expanded and paddled in short time to generate large thrust. In the retraction stroke, the webbed feet folded to reduce the resistance. The results showed that the prototype could finish the paddling gait.

Table 5 Webbed foot kinematic parameters

Symbol	Range	Concept	Unit
θ	[90,180]	Paddling angle per cycle	∘
T	[1.6,5.6]	Temporal baseline	s
t_1	[0.375,0.625]	Temporal scaling factor of power stroke	–
t_2	[0.125,0.375]	Temporal scaling factor of flexion phase	–
t_3	[0.375,0.625]	Temporal scaling factor of retraction stroke	–
t_4	[0.125,0.375]	Temporal scaling factor of extension phase	–

5 Surrogate Model of Hydrodynamics

This section investigated the influence of kinematic parameters on the propulsion efficiency of WIR-II. Based on discrete hydrodynamic computation data of webbed foot from a single paddling cycle, a surrogate model correlating kinematic parameters with propulsion efficiency was developed and analyzed.

5.1 Parameter Analysis of Motion

According to the Eqs. (11)-(14), once the geometric parameters of the mechanism are fixed, hydrodynamic performance becomes governed by velocity, which is related to the time and angle of each phase. To investigate the impact of the two factors on the effective thrust efficiency and find the best motion strategies, the variables were firstly defined as Table 5. A temporal baseline was introduced as the reference

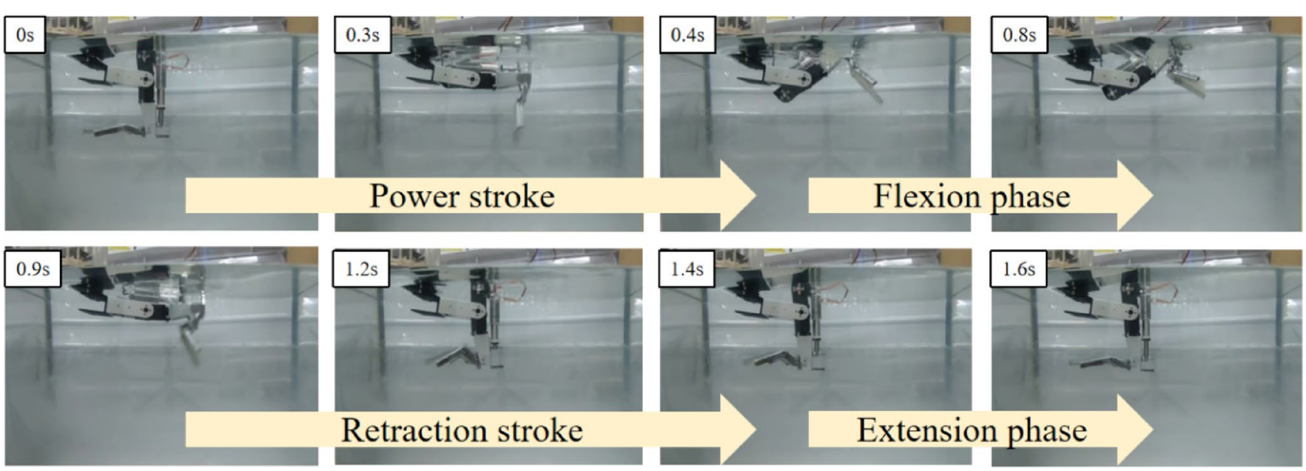

Fig. 16 The motion of the webbed feet in a cycle

Table 6 Factor-level assignments

Factor	t_1	t_2	t_3	t_4	T	θ
Level 1	0.375	0.125	0.375	0.125	1.6	90
Level 2	0.5	0.25	0.5	0.25	3.6	135
Level 3	0.625	0.375	0.625	0.375	5.6	180

Table 7 Orthogonal experiment assignments

Experiment ID	t_1	t_2	t_3	t_4	T	θ
1	1	1	1	1	1	1
2	1	1	2	1	2	3
3	1	2	1	3	3	2
…	…	…	…	…	…	…
16	3	2	3	1	3	1
17	3	3	1	3	2	1
18	3	3	2	3	1	3

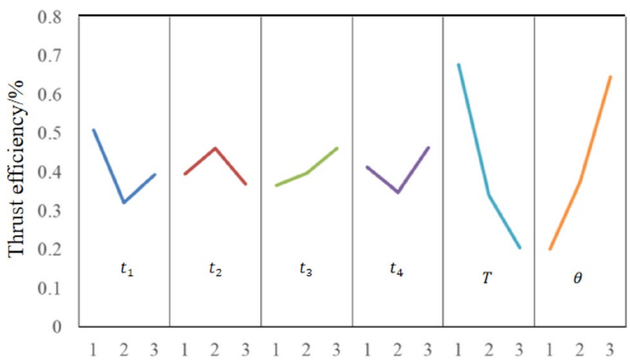

Fig. 17 Results of impact on the effective thrust efficiency of each factor

of the total cycle and the duration of each phase was calculated as the product of temporal baseline and temporal scaling factor of each phase.

The levels of all kinematic parameters for the webbed-foot mechanism were defined in Table 6. An orthogonal experiment was conducted by SPSSAU for parameters above, as shown in Table 7.

According to Table 7, simulations were carried out using different motion equations of webbed foot mechanism. Figure 17 showed the results of impact on the effective thrust efficiency of each factor. Paddling angle per cycle and temporal baseline demonstrated the dominant influences. Other factors including t_1, t_4, t_2, t_3 exhibited the descending order of impact. But each factor was non-negligible.

Table 8 Comparison of error between Co-Kriging and kriging

Model	Percentage of maximum error	Root mean square error
Kriging	4.77%	0.0213
Co-Kriging	4.65%	0.0188

5.2 Surrogate Model

A sampling method and training model should be selected. A comparative analysis of sampling methods is shown in Fig. 18, contrasting traditional Latin Hypercube Sampling (LHS) with optimized LHS employing the max-min distance criterion. The optimized LHS achieved superior spatial uniformity. This optimization transformed sampling to an optimization problem and eliminated reliance on orthogonal experiment. So, the optimized LHS was adopted.

This study employed Kriging regression to construct high-fidelity global models from limited samples. The core process of the Kriging surrogate model was to construct global approximator that exploited known sample points. Co-Kriging, which can be used for multi-varaiable or multi-fidelity datasets, was an extension of Kriging.

To ensure uniform coverage across the space, 60 levels for each factor were assigned in the fluid dynamics simulations (Typically ten times the number of design variables). The maximin-optimized LHS was employed to generate 60 sample points and effective thrust efficiency of each sample was obtained through fluid dynamics simulations, forming the training datasets fossr surrogate models. The results

Fig. 18 Comparison of sampling results between traditional LHS and optimized LHS

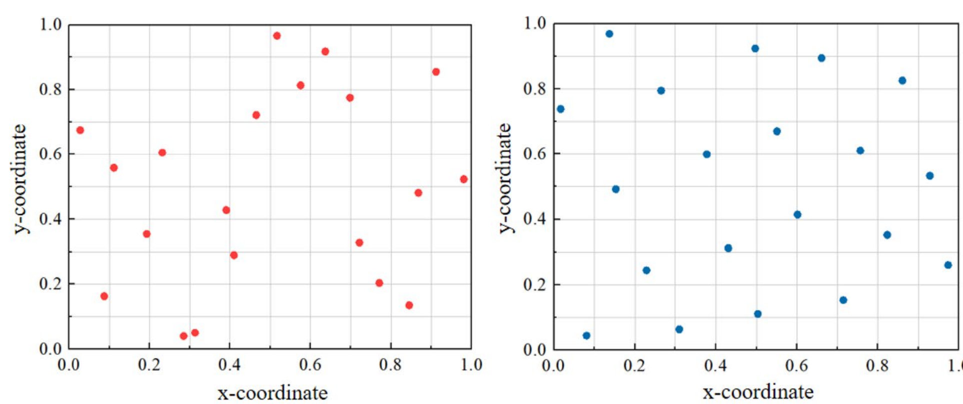

(a) traditional LHS (b) optimized LHS

of another 8 sample points were also obtained in the same way, forming the validating datasets. Both Kriging and Co-Kriging methods were tested and the results of prediction error are shown in Table 8. The maximum error was both less than 5%. Because Co-Kriging requires the estimation of additional hyperparameters, which increases model complexity, training time, and the risk of overfitting, especially given our limited dataset of high-fidelity CFD simulations. The negligible performance gain did not justify the significant increase in computational and operational complexity. Although Co-Kriging exhibited a marginally lower prediction error, the Kriging model was ultimately selected for its superior computational efficiency and simplicity.

Above all, the process of algorithm was as follows:

(1) Identify critical parameters governing thrust-specific efficiency through hydrodynamic analysis of the webbed-foot mechanism.
(2) Perform maximin-optimized LHS within the parameter space to generate the initial training datasets.
(3) Import the information about Simplified geometric model and defined motion equations to XFlow and conduct CFD simulations. Compute the effective thrust efficiency.
(4) Build Kriging-based surrogate models using training data and optimize training parameters to improve accuracy.
(5) Sample across the design space to generate validating datasets.
(6) Calculate RMSE between predictions and validating datasets. If RMSE is no more than 5%, model convergence achieved. Otherwise, merge the validating datasets with training datasets and conduct retraining.

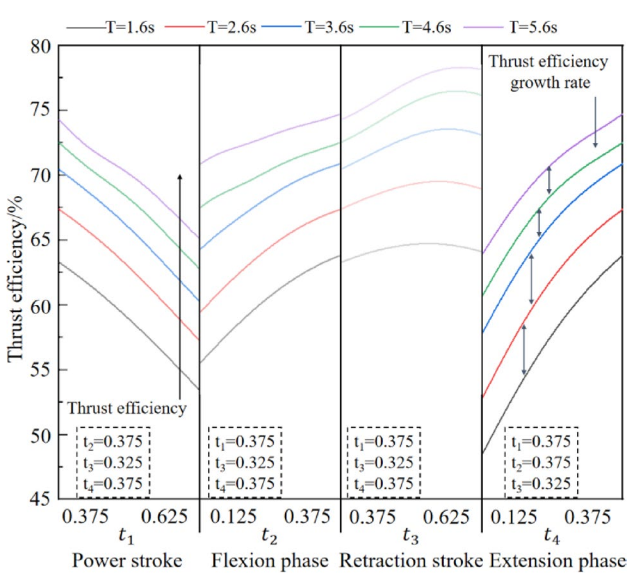

Fig. 19 Results of effective thrust efficiency under different temporal parameters(θ =180°)

(7) Repeat Steps (5)-(6) until RMSE is less than 5%.

5.3 Results

Figure 19 shows the results of effective thrust efficiency under different temporal parameters when paddling angle is 180° per cycle.

The slope of the curve in extension phase was the largest, which showed t_4 had the greatest impact. Similarly, t_1 ranked secondary in significance. t_2 and t_3 had marginal effects. As T increased, the efficiency rose while curve spacing reduces. This indicated the increase of T reduced influence of temporal scaling factor, especially t_2 and t_3. The impact of each temporal scaling factor was analyzed:

(1) For t_1: When T was fixed, efficiency increases as t_1 decreases. When T varies, the slope of each curve is the same, which indicates t_1 is independent of T.
(2) For t_2: When T was fixed, efficiency rose with higher t_2. The influence attenuates at larger t_2.
(3) For t_3: When T was fixed, maximum efficiency occurred at mid-range. The influence intensified at larger t_3.
(4) For t_4: When T was fixed, efficiency increased with larger t_1. And t_4 was also independent of T.

The influence of dual-factor on propulsion efficiency was also analyzed, as shown in Fig. 20. This study selected combinations of variables that exhibited a coupled influence. Figure 20(a) shows the impact of θ and t_1 on propulsion efficiency of the webbed foot. The low-efficiency region occurred under conditions of a smaller paddling angle combined with a longer power phase duration. Under these conditions, the paddling velocity of the webbed foot became very low, resulting in significantly reduced thrust. Meanwhile, the extended duration leads to greater energy dissipation in the flow field, further decreasing efficiency. Conversely, a larger paddling angle paired with a shorter power stroke duration made higher propulsion efficiency. Additionally, when the power stroke duration is fixed, increasing the paddling angle has a more substantial effect on improving propulsion efficiency, indicating that optimizing the paddling angle should be prioritized during parameter tuning.

Figure 20(b) shows the impact of θ and t_3 on propulsion efficiency of webbed feet. Variations in t_3 have a negligible impact on propulsion efficiency. When θ is held constant, the influence of t_3 on propulsion efficiency becomes even more marginal. The folded morphology of WIR-II resulted in a streamlined profile, which prevents significant changes in t_3 from substantially affecting detrimental drag. This

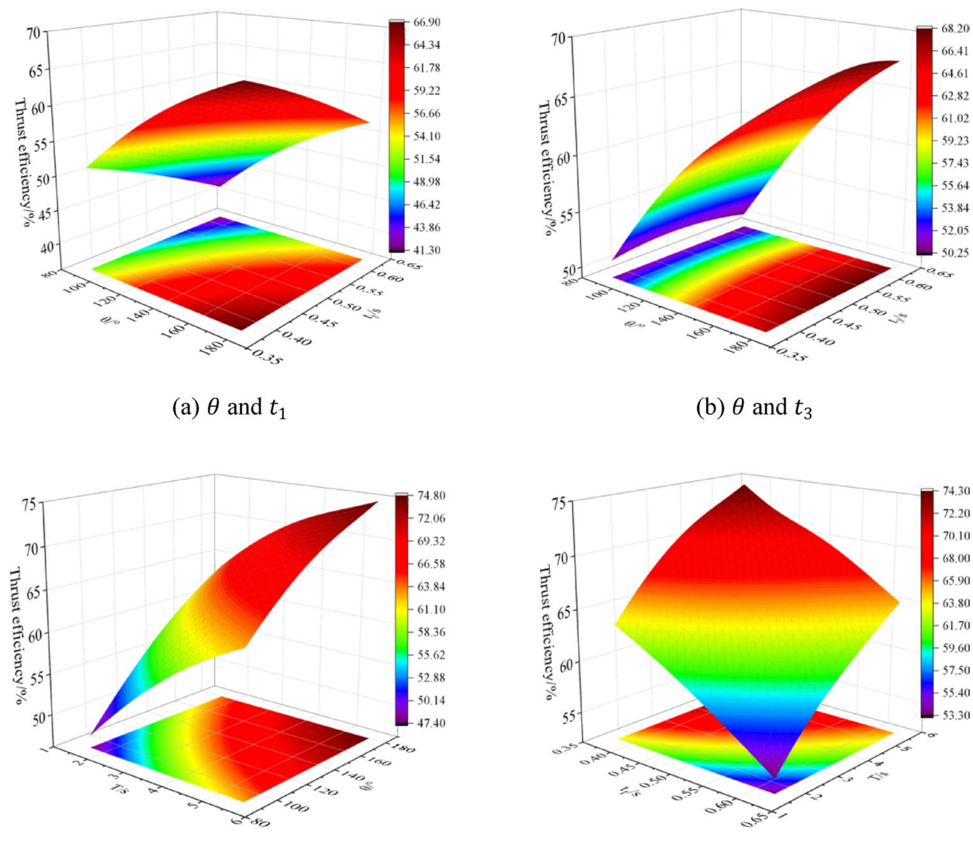

(a) θ and t_1 (b) θ and t_3 (c) T and θ (d) t_1 and T

Fig. 20 Results of effective thrust efficiency under coupling variables

Table 9 Optimization advice of each factor

Influence rank	Factor	Advice
1	θ	↑
2	T	↑
3	t_4	↑
4	t_1	↓
5	t_2	↑
6	t_3	-

same mechanism also explains its limited effect on overall propulsion efficiency.

Figure 20(c) shows the impact of T and θ on propulsion efficiency of webbed feet. The low-efficiency region occurred when both the paddling angle and power phase duration are relatively small. Conversely, the highest efficiency is achieved when both parameters are set to their maximum values within the range investigated in this study. Furthermore, the paddling angle has a greater influence on propulsion efficiency than the power phase duration. However, the improvement exhibited diminishing returns with further increases in T and θ .

Figure 20(d), shows the impact of t_1 and T on propulsion efficiency of webbed feet. The low-efficiency region occurred under conditions of a larger power stroke duration combined with a smaller paddling angle. Conversely, the high-efficiency region is achieved with a smaller power phase duration and a larger paddling angle. An excessively long power stroke duration meant its proportion within the overall cycle is too high, leading to increased energy dissipation within the flow field, that is, more energy failed to

Table 10 Kinematic parameters in different simulations

Simulation ID	t_1	t_2	t_3	t_4	T/s	θ /°
1	0.375	0.125	0.375	0.125	1.6	180
2	0.5	0.25	0.5	0.25	1.6	180
3	0.625	0.375	0.625	0.375	1.6	180
4	0.375	0.375	0.375	0.375	3.6	180
5	0.375	0.375	0.375	0.375	5.6	180
6	0.375	0.375	0.375	0.375	1.6	90
7	0.375	0.375	0.375	0.375	1.6	135
8	0.375	0.375	0.375	0.375	1.6	180

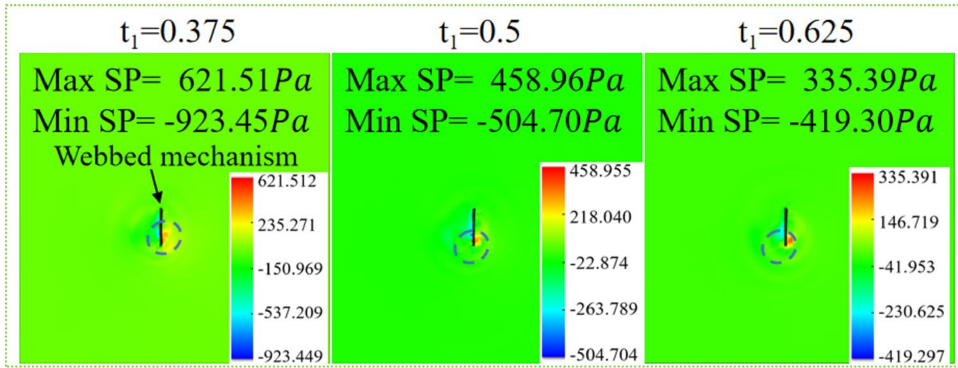

Fig. 21 Static pressure at cross-section $x=0$ under different t_1

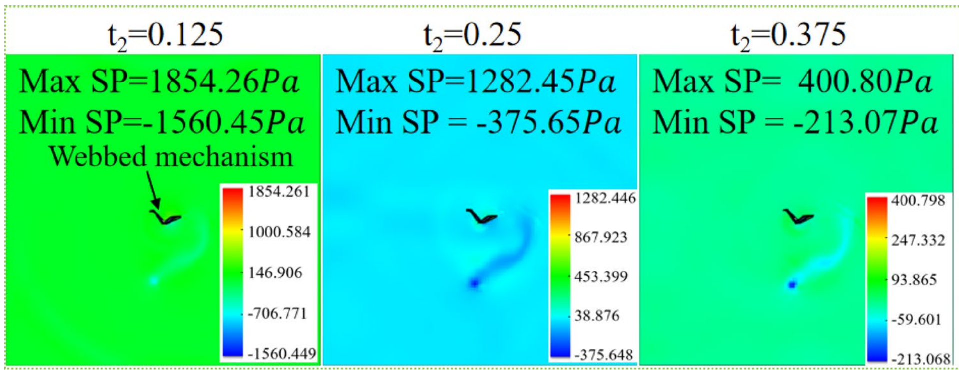

(a)

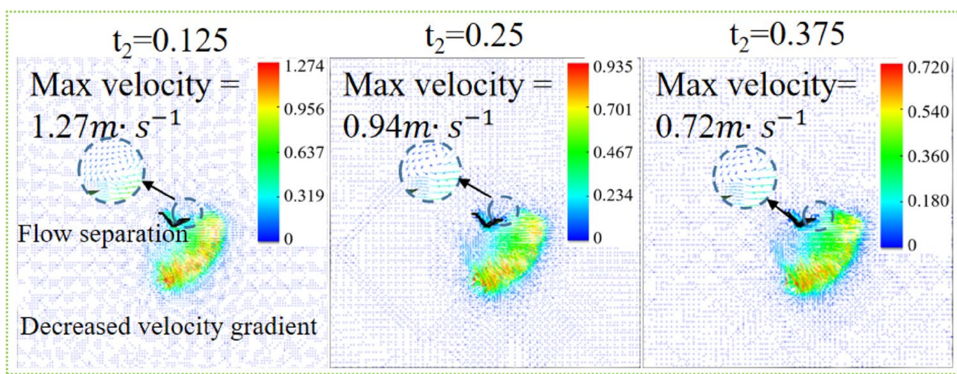

(b)

Fig. 22 Results at cross-section $x=0$ under different t_2 **a** static pressure **b** velocity vectors

contribute to propulsion, thereby reducing the overall propulsion efficiency.

Considering the trade-offs between efficiency and engineering feasibility, optimized parameter ranges are recommended in Table 9. Among them, the maximum T should be limited to ensure the motion velocity. Notice that all the advice should follow the parameter range which defined in Table 5.

To investigate the impact of the kinematic parameters on hydrodynamic field characteristics, the simulations shown in Table 10 were designed.

The influence of t_1 variation on the static pressure field is shown in Fig. 21. Comparative analysis was conducted for three critical values of t_1=0.375 (time is 0.3s), t_1=0.5 (time is 0.4s) and t_1=0.625 (time is 0.5s). The pressure differentials, which is the source of thrust, decreased as t_1 increased. The longer t_1 resulted in a reduction of the instantaneous velocity of paddling, thereby causing reduction of thrust. This trend is clearly illustrated by the progressively diminishing pressure differential shown in the static pressure distribution. Moreover, the longer t_1 means that more work is required to overcome fluid frictional resistance, that is, more of the input energy is consumed without contributing to propulsion. At the same time, the extended phase time allows the flow field to develop more fully, leading to the dissipation of some vortices, which further reduces the efficiency.

The influence of t_2 variation on the static pressure and velocity vectors is shown in Fig. 22. Comparative analysis was conducted for three critical values of t_2=0.125(time is 0.7s), t_2=0.25(time is 1 s) and t_2=0.375(time is 1.3s). Increasing t_2 reduced velocity gradients, but the area of wake separation basically unchanged. The slower motion leads to a decrease in the pressure differential across the surface of the foot. If the duration of this phase is longer, the next phase begins before the energy in the wake has fully dissipated, thereby obtained larger propulsive efficiency. However, diminishing returns emerged when further increasing value.

The influence of t_3 variation on the static pressure and velocity vectors is shown in Fig. 23. Comparative analysis was conducted for three critical values of t_3=0.375(time is 1.1s), t_3=0.5(time is 1.6s) and t_3=0.625(time is 2.1s). The flow separation area of t_3=0.375 case was less than that of others, but the pressure differentials was far larger. This phenomenon can be attributed to the flexion of WIR-II's webbed foot during this phase. Its more streamlined morphology means that even with reduced velocity, the pressure drag does not decrease significantly. Therefore, during parameter optimization, the priority of t_3 is relatively low.

The influence of t_4 variation on the static pressure and velocity vectors is shown in Fig. 24. Comparative analysis was conducted for three critical values of t_4=0.125(time is 1.5s), t_4=0.25(time is 2.2s) and t_4=0.375(time is 2.9s). Similar to retraction stroke, the pressure differentials area in extension phase was caused by the flow separation. Except the area of flow separation, velocity gradients and energy dissipation varied the same with retraction stroke as t_4 increased.

The influence of T variation on the static pressure and velocity vectors is shown in Fig. 25. Middle time of each

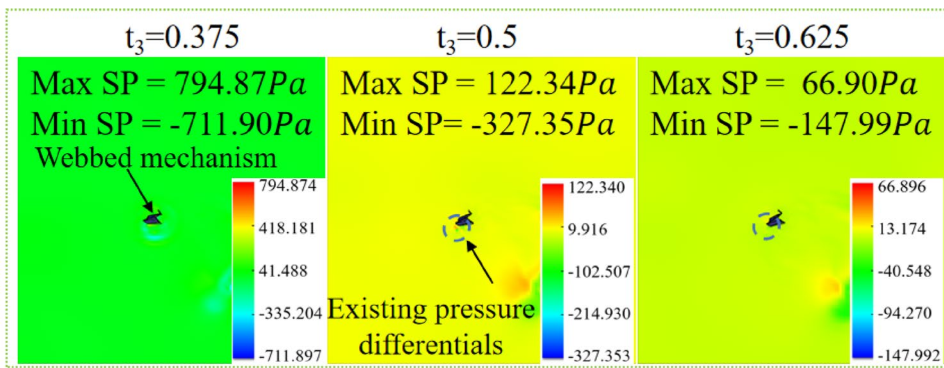

(a)

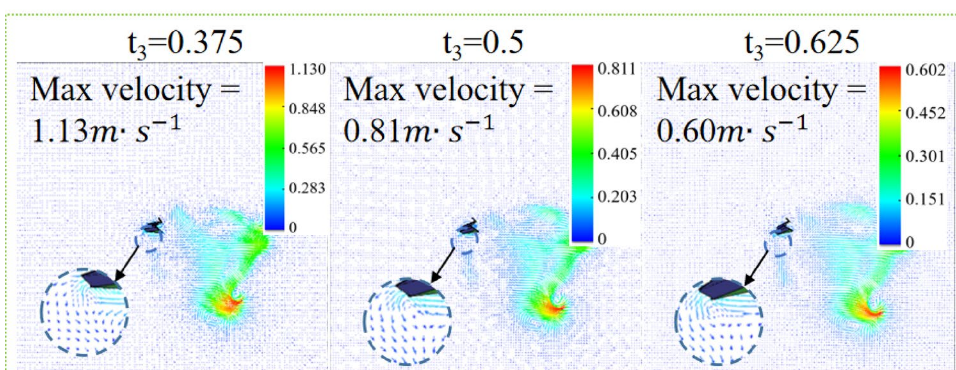

(b)

Fig. 23 Results at cross-section x=0 under different t_3 **a** static pressure **b** velocity vectors

Fig. 24 Results at cross-section $x=0$ under different t_4 **a** static pressure **b** velocity vectors

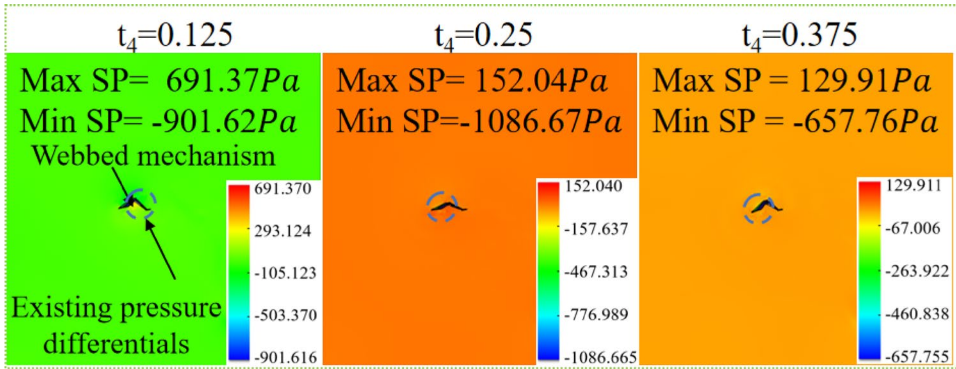

(a)

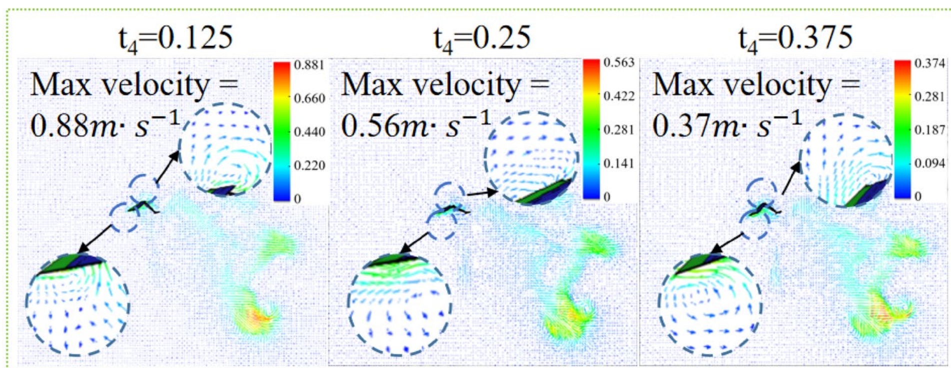

(b)

Fig. 25 Static pressure at cross-section x = 0 under different T

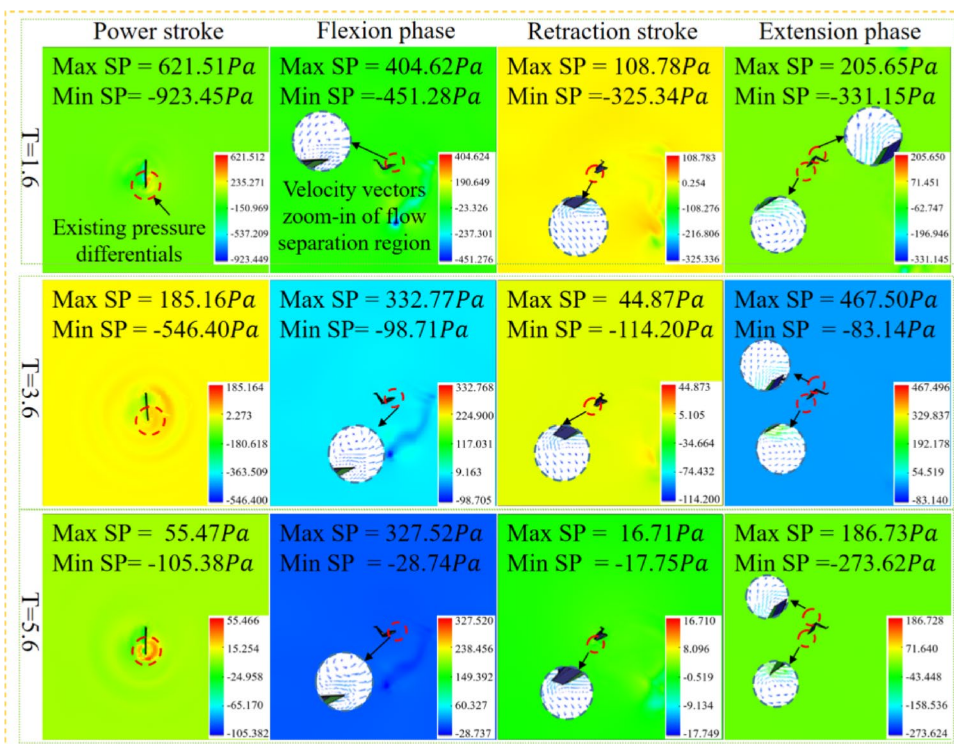

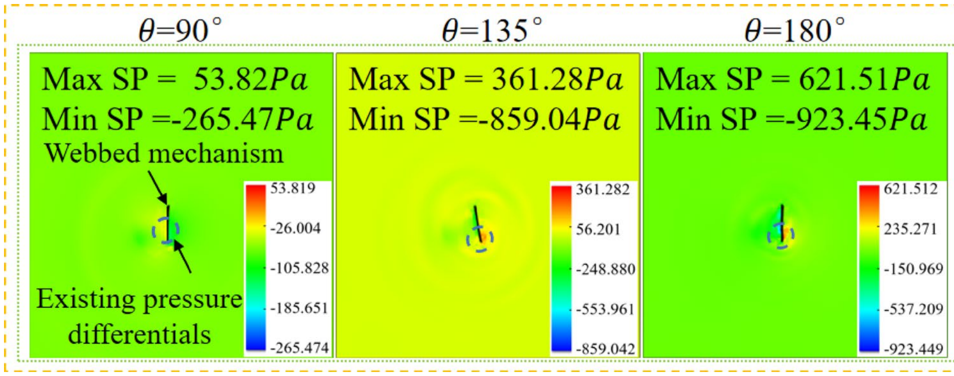

Fig. 26 Static pressure at cross-section $x=0$ under different θ

phase is selected to be compared. As T increased, the pressure differentials between windward and leeward sides in power stroke and the energy dissipation in other phase decreased. A longer cycle time allows the webbed foot to move with lower acceleration, which mitigates the inertial energy consumption required to accelerate both the foot itself and the added mass of water. Additionally, the extended cycle duration provides sufficient time for the flow field pressure and vortices to fully evolve and attain a stable state, thereby avoiding the underdevelopment and chaos flow field of short-period high-frequency motions and ultimately reducing energy dissipation. The suitable kinematic parameters can improve the flow adhesion but cannot eliminate flow separation.

The influence of θ variation on the static pressure is shown in Fig. 26. Comparative analysis was conducted for three critical values of $\theta=90^\circ$ (time is 0.55s), $\theta=135^\circ$ (time is 0.4s) and $\theta=180^\circ$ (time is 0.3s). A larger paddling angle results in a greater angle of attack, thereby enhancing the circulation around the webbed foot. This gives rise to a more stable leading-edge vortex. As a result, with the increase in the paddling angle, the maximum pressure differential progressively increases. Under a constant total cycle time, the greater pressure differential directed from the leeward side to the windward side generates increased thrust, thereby improving the overall propulsion efficiency.

Above all, more effective thrust can be obtained by increasing the pressure differentials between windward and leeward sides through increasing T, θ and t_1. Another way is to improve the flow adhesion and reduce the energy dissipation by increasing t_2, t_3 and t_4.

6 Conclusion

This paper proposed a novel webbed foot based on four-bar linkage mechanism with slider which can retract and fold simultaneously. The structural optimization through static analysis ensured the safety under working condition. The kinematic performance and reachable workspace was analyzed. The hydrodynamic performance of the propulsion mechanism was analyzed based on the Morison equation and CFD simulation models, characterized by an established thrust efficiency metric. The simulation results indicate the webbed foot proposed in this paper reduce detrimental drag during the retraction stroke, but increased energy dissipation occurs due to flow separation. So, the impact on the thrust efficiency of each kinematic parameters should be studied. So, a surrogate model was developed correlating the webbed-foot mechanism's kinematic parameters including paddling angle per cycle, temporal baseline, and temporal scaling factor of power stroke, flexion phase, retraction stroke, and extension phase with the thrust efficiency. Results demonstrate that the metric decreased with rising temporal scaling factor of power stroke but increased with rising other parameters. Parameter influence hierarchy should be paddling angle per cycle, temporal baseline, and temporal scaling factor, whose impact gradually decreases. Flow field analysis shows that paddling angle per cycle and temporal scaling factor of power stroke enhance thrust by increasing pressure differentials and other parameters reduce dissipation by improving flow attachment. This can supply theoretical reference of gait optimization.

In future, the propulsion mechanism need to be further improved to enhance flow attachment during underwater motion, thereby increasing locomotive stability. Comprehensive evaluation metrics will be established by integrating other locomotive behaviors of the bionic aquatic bird robot, such as bipedal locomotion and diving motion.

Authors' Contributions Yan Niu: Investigation, Methodology, Simulation, Visualization, Writing—original draft, review & editing. Xinru Lin: Investigation, Methodology, Simulation, Visualization, Writing—review & editing. Shuxiang Guo: Funding acquisition, Project administration, Resources. Zhinbin Song: Funding acquisition, Project administration, Resources. Liwei Shi: Conceptualization, Supervision, Project administration, Funding acquisition, Resources.

Funding This work was supported by National Natural Science Foundation of China (62273042, 61773064) and the Fundamental Research Funds for the Central Universities (2025CX01016).

Data Availability Data sets generated during the current study are available from the corresponding author on reasonable request.

Declarations

Conflict of interest The authors declare that they have no known competing financial interests or personal relationships that could have appeared to influence the work reported in this paper.

Ethical Approval and Consent to Participate This study was conducted in compliance with ethical standards and guidelines. All participants provided informed consent prior to their involvement in the study, and their confidentiality and privacy were strictly maintained throughout the research process.

Consent for Publication All authors have reviewed and approved the manuscript and consent to its publication in Journal of Bionic Engineering. If applicable, consent for publication has also been obtained from all participants involved in the study.

References

1. Bai, X., Shang, J., Luo, Z., Jiang, T., & Yin, Q. (2022). Development of amphibious biomimetic robots. *Journal of Zhejiang University-Science A (Applied Physics & Engineering)*, *23*(3), 157–187. https://doi.org/10.1631/jzus.A2100137
2. Bao, P., Shi, L., Duan, L., Guo, S., & Li, Z. (2023). A review: From aquatic lives locomotion to bio-inspired robot mechanical designations. *Journal of Bionic Engineering, 20*(6), 2487–2511. https://doi.org/10.1007/s42235-023-00421-2
3. Ma, S., Qin, F., Chen, S., Li, L., Wang, J., Wang, Z., Li, S., & Xiao, X. (2023). Self-adaptive rolling motion for snake robots in unstructured environments based on torque control. *Biomimetic Intelligence and Robotics*, *3*(3), 100117. https://doi.org/10.1016/j.birob.2023.100117
4. Wang, X., Zhao, J., Pei, X., Wang, T., Hou, T., & Yang, X. (2024). Bioinspiration review of aquatic unmanned aerial vehicle (AquaUAV). *Biomimetic Intelligence and Robotics*, *4*(2), 100154. https://doi.org/10.1016/j.birob.2024.100154
5. Liu, R., Hu, X., Jiang, Z., Wang, J., & Zhang, W. (2025). Survey on heterogeneous aquatic robot systems: Communication, perception, navigation, control, decision-making and energy management. *Robot Learn, 2*(1), Article 0003. https://doi.org/10.55092/rl20250003
6. Ijspeert, A. J., Crespi, A., Ryczko, D., & Cabelguen, J. M. (2007). From swimming to walking with a salamander robot driven by a spinal cord model. *Science*, *315*(5817), 1416–1420. https://doi.org/10.1126/science.1138353
7. Hopkins, J. K., Spranklin, B. W., & Gupta, S. K. (2009). A survey of snake-inspired robot designs. *Bioinspiration & Biomimetics, 4*(2), Article 21001. https://doi.org/10.1088/1748-3182/4/2/021001
8. Crespi, A., Badertscher, A., Guignard, A., & Ijspeert, A. J. (2005). AmphiBot I: An amphibious snake-like robot. *Robotics and Autonomous Systems*, *50*(4), 163–175. https://doi.org/10.1016/j.robot.2004.09.015
9. Sverdrup-Thygeson, J., Kelasidi, E., Pettersen, K. Y., & Gravdahl, J. T. (2018). The underwater swimming manipulator-a bioinspired solution for subsea operations. *IEEE Journal of Oceanic Engineering*, *43*(2), 402–417. https://doi.org/10.1109/joe.2017.2768108
10. Li, D., Pan, Z., Deng, H., & Peng, T. (2020). 2D underwater obstacle avoidance control algorithm based on IB-LBM and APF method for a Multi-Joint Snake-Like robot. *Journal of Intelligent & Robotic Systems*, *98*(3–4), 771–790. https://doi.org/10.1007/s10846-019-01097-9
11. Crespi, A., Karakasiliotis, K., Guignard, A., & Ijspeert, A. J. (2013). *Salamandra robotica* II: An amphibious robot to study salamander-like swimming and walking gaits. *IEEE Transactions on Robotics, 29*(2), 308–320. https://doi.org/10.1109/tro.2012.2234311
12. Karakasiliotis, K., Thandiackal, R., Melo, K., Horvat, T., Mahabadi, N. K., Tsitkov, S., Cabelguen, J. M., & Ijspeert, A. J. (2016). From cineradiography to biorobots: An approach for designing robots to emulate and study Animal locomotion. *Journal of the Royal Society Interface, 13*(119), 20151089. https://doi.org/10.1098/rsif.2015.1089
13. Meng, Y., Wu, Z., Dong, H., Wang, J., & Yu, J. (2022). Toward a novel robotic Manta with unique pectoral fins. *IEEE Transactions on Systems, Man, and Cybernetics-Systems, 52*(3), 1663–1673. https://doi.org/10.1109/tsmc.2020.3034503
14. Xia, M., Wang, H., Yin, Q., Shang, J., Luo, Z., & Zhu, Q. (2023). Design and mechanics of a composite wave-driven soft robotic fin for biomimetic amphibious robot. *Journal of Bionic Engineering*, *20*(1), 934–952. https://doi.org/10.1007/s42235-022-00328-4
15. He, Y., Shi, L., Guo, S., Pan, S., & Wang, Z. (2016). Preliminary mechanical analysis of an improved amphibious spherical father robot. *Microsystem Technologies*, *22*(8), 2051–2066. https://doi.org/10.1007/s00542-015-2504-9
16. Bao, P., Hu, Y., Shi, L., Guo, S., & Li, Z. (2022). A decoupling three-dimensional motion control algorithm for spherical underwater robot. *Biomimetic Intelligence and Robotics*, *2*(3), 100067. https://doi.org/10.1016/j.birob.2022.100067
17. Guo, S., He, Y., Shi, L., Pan, S., Xiao, R., Tang, K., & Guo, P. (2018). Modeling and experimental evaluation of an improved amphibious robot with compact structure. *Robotics and Computer-Integrated Manufacturing*, *51*, 37–52. https://doi.org/10.1016/j.rcim.2017.11.009
18. Shi, L., Zhang, Z., Li, Z., Guo, S., Pan, S., Bao, P., & Duan, L. (2022). Design, implementation and control of an amphibious spherical robot. *Journal of Bionic Engineering*, *19*(6), 1736–1757. https://doi.org/10.1007/s42235-022-00229-6
19. Shi, L., Hu, Y., Su, S., Guo, S., Xing, H., Hou, X., Liu, Y., Chen, Z., Li, Z., & Xia, D. (2020). A fuzzy PID algorithm for a novel miniature spherical robots with three-dimensional underwater motion control. *Journal of Bionic Engineering*, *17*(5), 959–969. https://doi.org/10.1007/s42235-020-0087-3
20. Algeldinger, T. L., & Fish, F. E. (1995). Hydroplaning by ducklings-overcoming limitations to swimming at the water-surface. *Journal of Experimental Biology*, *198*(7), 1567–1574. https://doi.org/10.1242/jeb.198.7.1567
21. Ribak, G., Swallow, J. G., & Jones, D. R. (2010). Drag-based 'hovering' in ducks: The hydrodynamics and energetic cost of bottom feeding. *PLoS One, 5*(9), e12565. https://doi.org/10.1371/journal.pone.0012565
22. Ribak, G., & Gurka, R. (2023). The hydrodynamic performance of Duck feet for submerged swimming resembles oars rather than delta-wings. *Scientific Reports*, *13*, 16217. https://doi.org/10.1038/s41598-023-42784-w
23. Huang, J., Wang, T., Liang, J., Yang, X., Wang, H., & Kang, G. (2023). Biorobotic waterfowl flipper with skeletal skins in a computational framework: Kinematic conformation and hydrodynamic analysis. *Advanced Intelligent Systems*, *5*, 2200380. https://doi.org/10.1002/aisy.202200380
24. Pandey, J., Reddy, N. S., Ray, R., & Shome, S. N. (2013). Biological swimming mechanism analysis and design of robotic frog, *In*: *Proceedings of* 10*th IEEE international conference on mechatronics and automation* (*ICMA*). Takamatsu, Japan, pp 1726–1731. https://doi.org/10.1109/ICMA.2013.6618176

25. Chen, G., Ti, X., Shi, L., & Hu, H. (2022). Design of beaver-like Hind limb and analysis of two swimming gaits for underwater narrow space exploration. *Journal of Intelligent & Robotic Systems*, *104*(4), 65. https://doi.org/10.1007/s10846-022-01610-7
26. Kashem, S. B. A., Jawed, S., Ahmed, J., & Qidwai, U. (2019). Design and implementation of a quadruped amphibious robot using duck feet. *Robotics, 8*(3), 77. https://doi.org/10.3390/robotics8030077
27. Song, Z., Zhang, Y., Wu, Y., Li, S., Zhao, L., Cao, H., Kang, R., Shi, L., & Dai, J. (2025). A new reciprocating straight propulsion for high propulsive hydrodynamic efficiency. *Mechanism and Machine Theory, 205*, Article 105833. https://doi.org/10.1016/j.mechmachtheory.2024.105833
28. Chen, G., Tu, J., Ti, X., Wang, Z., & Hu, H. (2021). Hydrodynamic model of the beaver-like bendable webbed foot and paddling characteristics under different flow velocities. *Ocean Engineering*, *234*, 109179. https://doi.org/10.1016/j.oceaneng.2021.109179
29. Huang, C., & Liu, M. (2020). Modeling hydrate-bearing sediment with a mixed smoothed particle hydrodynamics. *Computational Mechanics*, *66*(4), 877–891. https://doi.org/10.1007/s00466-020-01895-1
30. Chen, G., Wang, P. W., Tu, Z., Hu, J., Wang, H., Cheng, D. H., & Zhu, L. (2023). Modeling of swimming posture dynamics for a beaver-like robot. *Ocean Engineering*, *279*, 114550. https://doi.org/10.1016/j.oceaneng.2023.114550
31. Zhang, D., Wang, Z., Ling, H., & Zhu, X. (2021). Kriging-based shape optimization framework for blended-wing-body underwater glider with NURBS-based parametrization. *Ocean Engineering*, *219*(58), 108212. https://doi.org/10.1016/j.oceaneng.2020.108212
32. Chen, H., Li, W., & Cui, W. (2023). Surrogate-assisted evolutionary algorithm with hierarchical surrogate technique and adaptive infill strategy. *Expert Systems with Applications, 232*(12), 120826. https://doi.org/10.1016/j.eswa.2023.120826
33. Uribe, D., Baudouin, C., Durand, C., & Bigot, R. (2023). Predictive control for a single-blow cold upsetting using surrogate modeling for a digital twin. *International Journal of Material Forming*, 17, Article 7. https://doi.org/10.1007/s12289-023-01803-x
34. Abouhussein, A., & Peet, Y. T. (2023). Optimized hydrodynamic interactions in phalanx school arrays of accelerated thunniform swimmers. *Physica Scripta, 98*(3), Article 16. https://doi.org/10.1088/1402-4896/acb859
35. Grimstad, B., Foss, B., Heddle, R., & Woodman, M. (2016). Global optimization of multiphase flow networks using spline surrogate models. *Computers & Chemical Engineering*, *84*(1), 237–254. https://doi.org/10.1016/j.compchemeng.2015.08.022
36. Fan, J., Eves, J., Thompson, H. M., Toropov, V. V., Kapur, N., Copley, D., & Mincher, A. (2011). Computational fluid dynamic analysis and design optimization of jet pumps. *Computers & Fluids*, *46*(1), 212–217. https://doi.org/10.1016/j.compfluid.2010.10.024
37. Liu, Q., Chen, H., Guo, P., Su, G., Li, W., Zeng, X., Fan, D., & Cui, W. (2024). Unified scheme design and control optimization of flapping wing for next-generation Manta ray robot. *Ocean Engineering*, *309*(2), 118487. https://doi.org/10.1016/j.oceaneng.2024.118487
38. Gao, W., Gu, H., Feng, M., Sun, Y., & Zhao, Z. (2021). Parameter design and optimization of underwater vehicle rudder wing. *Journal of Ocean Technology, 40*(04), 74–83. https://doi.org/10.3969/j.issn.1003-2029.2021.04.010
39. Liu, H., Shi, L., Guo, S., Xing, H., Hou, X., & Liu, Y. (2018). Platform design for a natatores-like amphibious robot, In: Proceedings of. IEEE international conference on mechatronics and automation (ICMA), Changchun, China, 2018, pp 1627–1632. https://doi.org/10.1109/ICMA.2018.8484387
40. Liu, H., Li, Z., Hu, Y., Shi, L., Guo, S., Hou, X., Xing, H., Liu, Y., & Xia, D. (2019). Hydrodynamic analysis of webbed foot for a novel biomimetic robotic duck, *In*: *Proceedings of the 15th IEEE International Conference on Advanced Robotics and Its Social Impacts* (*IEEE ARSO*). Beijing, China, 45–50. https://doi.org/10.1109/ARSO46408.2019.8948753
41. Ribak, G., Weihs, D., & Arad, Z. (2004). How do cormorants counter buoyancy during submerged swimming? *Journal of Experimental Biology*, *207*(12), 2101–2114. https://doi.org/10.1242/jeb.00997